

NANO EXPRESS

Open Access



A Ternary Magnetic Recyclable ZnO/Fe₃O₄/g-C₃N₄ Composite Photocatalyst for Efficient Photodegradation of Monoazo Dye

Zhansheng Wu^{1,2*}, Xiaoqing Chen², Xiaochen Liu¹, Xia Yang¹ and Yan Yang¹

Abstract

To develop a highly efficient visible light-induced and conveniently recyclable photocatalyst, in this study, a ternary magnetic ZnO/Fe₃O₄/g-C₃N₄ composite photocatalyst was synthesized for the photodegradation of Monas dye. The structure and optical performance of the composite photocatalyst were characterized using X-ray diffraction (XRD), transmission electron microscopy (TEM), energy dispersive spectroscopy (EDS), photoluminescence (PL) spectra, ultraviolet–visible diffuse reflection, and photo-electrochemistry. The photocatalytic activities of the prepared ZnO/Fe₃O₄/g-C₃N₄ nanocomposites were notably improved, and they were significantly higher than those of pure g-C₃N₄ and ZnO. Given the presence of the heterojunction between the interfaces of g-C₃N₄ and ZnO, the higher response to visible light and separation efficiency of the photo-induced electrons and holes enhanced the photocatalytic activities of the ZnO/Fe₃O₄/g-C₃N₄ nanocomposites. The stability experiment revealed that ZnO/Fe₃O₄/g-C₃N₄-50% demonstrates a relatively higher photocatalytic activity after 5 recycles. The degradation efficiency of MO, AYR, and OG over ZnO/Fe₃O₄/g-C₃N₄-50% were 97.87%, 98.05%, and 83.35%, respectively, which was due to the number of dye molecules adsorbed on the photocatalyst and the structure of the azo dye molecule. Azo dyes could be effectively and rapidly photodegraded by the obtained photocatalyst. Therefore, the environment-friendly photocatalyst could be widely applied to the treatment of dye contaminated wastewater.

Keywords: ZnO, g-C₃N₄, Photocatalytic degradation, Methyl orange

Introduction

As a major global environmental issue, a significant amount of pollutants is discharged into the lakes, rivers, and ground water due to rapid industrialization, which leads to water pollution. It was estimated that approximately 10–15% of organic dyes are discharged, which has carcinogenic and mutagenic effects on humans [1]. Therefore, methods that degrade industrial waste water, particularly organic dyes, are currently under investigation by researchers. Among various methods, the use of a photocatalytic technology with photocatalysts to degrade environmental pollutants was considered a potential approach [2, 3].

Furthermore, ZnO is one of the most widely used photocatalysis, given its high photosensitivity, low-cost, and environmentally friendly nature [4, 5]. However, pure ZnO is subject to three major drawbacks. First, it can only absorb ultraviolet (UV) light of solar energy with a wavelength less than 368 nm due to its wide band gap (3.37 eV), which limits its practical applications when sunlight is the energy source [6]. Second, a faster recombination of its photogenerated electron-hole pairs leads to a lower photocatalytic activity [7]. Third, the re-collection of ultrafine ZnO nanoparticles from the waste water using filtration and centrifugation is difficult to achieve, which limits its large-scale practical applications in the industry. Hence, in recent years, there were several attempts to develop multi-functional photocatalysts based on ZnO nanomaterials, with a high recyclability and excellent photocatalytic performances in the UV and visible irradiation ranges.

* Correspondence: wuzhans@126.com

¹School of Environmental and Chemical Engineering, Xi'an Polytechnic University, Xi'an 710048, People's Republic of China

²School of Chemistry and Chemical Engineering, Shihezi University, Shihezi 832003, People's Republic of China

Different strategies were therefore implemented to overcome the first and second drawbacks of ZnO, such as doping, surface modification with metal nanoparticles, and the development of heterostructure [8–10]. Among these, coupling ZnO with a narrow band gap semiconductor with high conduction band (CB) can effectively increase the range of light absorption and accelerate the separation rate of the electron-hole pairs. Graphite-like carbon nitride (g-C₃N₄), which has a band gap of 2.70 eV, was explored as a promising metal-free material for the conversion of solar energy into electricity or chemical energy [11, 12]. Moreover, it attracted significant attention due to its excellent photocatalytic performance, chemical and thermal stabilities, and favorable electronic structure, given the strong covalent bonds between the carbon and nitrogen atoms. However, a high recombination rate of photo-induced electron-hole pairs limited its enhanced photocatalytic performance [13]. Wide-bandgap semiconductors could be combined with g-C₃N₄ to achieve improved charge separation [7, 14, 15]. Based on the abovementioned methods, the combination of ZnO (wide-bandgap semiconductor) and g-C₃N₄ (narrow bandgap semiconductor) as a composite photocatalyst prevents the recombination of photogenerated electron-hole pairs and extends the light-absorption range of ZnO to the visible light spectrum. However, in most of the reported works, ZnO/g-C₃N₄ photocatalysts have low catalytic performance and are difficult to recover and reuse. Fortunately, Fe₃O₄ was widely used in the preparation of magnetic photocatalysts, due to its good magnetic low-cost, good stability, and environment-friendly nature [16]. Hence, the preparation of novel visible-light-driven magnetic ZnO/Fe₃O₄/g-C₃N₄ photocatalysts is significant, and it is important to further improve the photocatalytic efficiency. In addition, how the structure of monoazo dyes affects the photodegradation process of the photocatalyst has not been reported yet. So it is very interesting to explore and provide a reliable

theoretical basis for the application of photocatalysts in the efficient and fast treatment of dye wastewaters.

In this study, a novel and efficient photocatalyst of ZnO/Fe₃O₄/g-C₃N₄ nanocomposites was successfully prepared. The crystal structure, chemical states, and optical properties of the photocatalyst were characterized using X-ray diffraction (XRD), transmission electron microscopy (TEM), energy dispersive spectroscopy (EDS), X-ray photoelectron spectroscopy (XPS), photoluminescence (PL), vibrating sample magnetometry (VSM), and UV-vis diffuse reflectance spectroscopy (DRS). The photocatalytic performance of the photocatalyst was investigated by its degradation of methyl orange (MO) under visible light irradiation. The degradation of different monoazo dyes (MO, alizarin yellow R (AYR), and orange G (OG)) over ZnO/Fe₃O₄/g-C₃N₄ was also investigated. Moreover, to further evaluate the possible mechanism of the photocatalytic degradation of azo dyes, a free radical capture experiment and PL technique were employed.

Materials and Methods

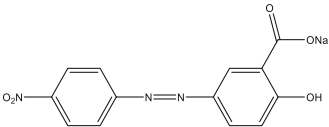
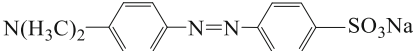
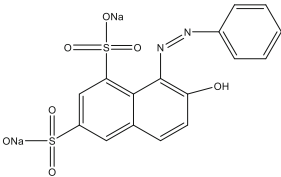
Materials

Zinc acetate was supplied by Tianjin Fuchen Chemical Reagent Co., Ltd. (Tianjin, China); ethanol (EtOH) (anhydrous alcohol) was purchased from Tianjin Fuyu Fine Chemical Co., Ltd. (Tianjin, China); urea and oxalic acid were obtained from the Tianjin Shengao Chemical Industry Co., Ltd. (Tianjin, China); and MO, AYR, and OG were provided by Tianjin Yongsheng Fine Chemical Co., Ltd. (Tianjin, China). The selected properties of MO, AYR, and OG are presented in Table 1.

Preparation of Fe₃O₄

For the preparation of Fe₃O₄, 0.540 g of FeCl₃·6H₂O and 0.278 g of FeSO₄·7H₂O (molar ratio 2:1) were dissolved in 40 mL of water. After 30 min of sonication, a brownish yellow solution was obtained and transferred to a

Table 1 Selected properties of azo dyes

Azo dyes	Structure	Formula	Molecular weight (g/mol)	Number of Sulfonic acid
AYR		C ₁₃ H ₉ N ₃ NaO ₅	309.21	0
MO		C ₁₄ H ₁₄ N ₃ SO ₃ Na	327.33	1
OG		C ₁₆ H ₁₀ N ₂ Na ₂ O ₇ S ₂	452.37	2

100-mL flask. Thereafter, the solution was stirred at 70 °C for 60 min in a nitrogen atmosphere, after which, 5 mL of aqueous ammonia (25%) was added to the solution under stirring. The obtained dark brown suspension was stirred for an additional 60 min and washed twice using water and ethanol, successively. The solid was then separated from the liquid phase using a magnetic field. The prepared dark brown sample was dried in a vacuum oven at 40 °C for 12 h.

Preparation of ZnO/Fe₃O₄

The photocatalyst was prepared based previous studies [17]. In a representative synthesis, solution A was prepared using the method that involves the dissolution of zinc acetate (2.196 g) in ETOH (60 mL) and stirring at 60 °C in a water bath for 30 min. Moreover, solution B was obtained by adding 5.040 g of oxalic acid solution to 80 mL of ETOH under stirring at 50 °C for 30 min. Solution B was then added dropwise to the warm solution A and stirred continuously at room temperature for 1 h to obtain the sol. Thereafter, to obtain a homogenous gel, the sol was aged in a sealed environment for a period of time. The product was dried for 24 h in a vacuum oven at 80 °C. Finally, ZnO was obtained by thermal treatment at 400 °C for 2 h. To prepare ZnO/Fe₃O₄, 0.12 g of Fe₃O₄ was dispersed in solution A.

Preparation of ZnO/Fe₃O₄/g-C₃N₄

For the preparation of ZnO/Fe₃O₄/g-C₃N₄, a homogeneous mixture was obtained by vigorously grinding 1 g of ZnO/Fe₃O₄ and melamine with a mass ratio of 1:1 and then dispersing the mixture in 20 ml of deionized water. The suspension was ultrasonicated for 1 h. Thereafter, the precursors were dried at 70 °C overnight to remove the solvent, and then the obtained solid was annealed at 550 °C for 2 h in air. The magnetic ZnO/Fe₃O₄/g-C₃N₄-50% composite was then successfully obtained. The amount of g-C₃N₄ was adjusted by controlling the amount of melamine (0.25 g, 1 g, and 2.3 g) during the preparation of the ZnO/Fe₃O₄/g-C₃N₄ nanocomposites, and the relevant products were denoted as ZnO/Fe₃O₄/g-C₃N₄-20%, ZnO/Fe₃O₄/g-C₃N₄-50%, and ZnO/Fe₃O₄/g-C₃N₄-70%, respectively.

Characterization Methods

The XRD spectra of the samples were analyzed using an Rigaku Giegerflex D/Max B diffractometer with Cu-K α radiation. The TEM was conducted together using a Tecnai G2F20 (USA) microscope. EDS spectra were performed by using an energy-dispersive X-ray spectrometer (EDS) attached to the TEM instrument. A surface area analyzer (Micromeritics, ASAP-2020, USA) was used to characterize the pore volume, pore size distribution, and specific surface area of the samples under N₂

adsorption at 77 K. To determine the optical band gap of the photocatalysts, the UV-visible absorption spectrum was obtained using a UV-Visible spectrophotometer with a reflectance standard of BaSO₄ (Hitachi UV-4100, Japan). The surface composition and chemical states of the samples were investigated using XPS (250XI ESCA) equipped with an Mg K α X-ray source (1253.6 eV). The PL spectra of the samples were determined using a fluorescence spectrophotometer (FLsp920, England) at room temperature, with an Xe lamp as an excitation light source. Photoelectrochemical measurements were conducted in three-electrode quartz cells with a 0.1-M Na₂SO₄ electrolyte solution. Platinum wire was used as the counter electrode, and Ag/AgCl were used as the reference electrodes, respectively. The working electrode was prepared as follows: 10 mg of the as-prepared photocatalyst was suspended in 1 mL of deionized water, which was then dip-coated onto a indium-tin oxide (ITO) glass electrode with dimensions of 10 mm \times 20 mm and then dried under an infrared lamp.

Photocatalytic Activity for Azo Dye

Photocatalytic experiments were conducted using a 500-W Xe lamp with a 420-nm cut-off filter at 25 °C, to study the visible light degradation of the MO, AYR, and OG solutions. In a traditional test, 10 mg of catalyst was added to 50 mL of azo dye solution (30 mg/L). The mixture was kept in the dark for 30 min to promote the adsorption of azo dye on the surface of the photocatalyst. The mixture was then irradiated under an Xe lamp to degrade the azo dye. After the degradation experiment, each sample was filtered with a 0.45- μ m filter membrane to remove the photocatalyst particles for analysis, and the concentrations of MO, AYR, and OG in the supernatant liquid were measured using a UV-5100 N spectrophotometer at λ_{max} = 466 nm, 373 nm, and 475 nm, respectively. The degradation efficiency (η) of the azo dye was calculated as follows:

$$\eta = \frac{C_0 - C_t}{C_0} \times 100\%$$

where C_0 and C_t are the concentrations of the azo dye at the initial and specified irradiation times, respectively.

Results and Discussion

XRD

X-ray diffraction (XRD) analysis was used to study the phase structures of the ZnO, g-C₃N₄, and ZnO/Fe₃O₄/g-C₃N₄ composites with different g-C₃N₄ loadings. The results are presented in Fig. 1. The peaks of the ZnO samples located at 2θ = 31.81°, 34.44°, 36.21°, 47.60°, 56.62°, 63.01°, and 67.97° correspond to the (100), (002), (101), (102), (110), (103), and (112) crystal planes of the

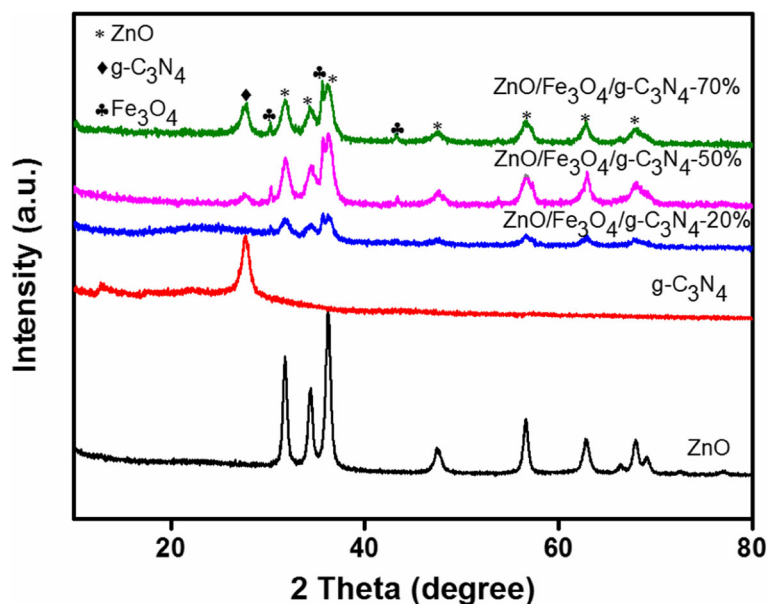


Fig. 1 XRD patterns of ZnO, g-C₃N₄, ZnO/Fe₃O₄/g-C₃N₄-20%, ZnO/Fe₃O₄/g-C₃N₄-50%, and ZnO/Fe₃O₄/g-C₃N₄-70%

hexagonal wurtzite structure of ZnO. All relevant diffraction data for the ZnO were in good agreement with the JCPDS 36-145 [17]. The strongest peak of the g-C₃N₄ sample corresponds to the (002) plane of its layer structure at $2\theta = 27.3^\circ$. As reported, the g-C₃N₄ structure has a weak diffraction peak at $2\theta = 13.2^\circ$, which is attributed to the (100) crystal plane of g-C₃N₄. The width of the diffraction peak decreased, which indicates the influence of geometric constraints on the nanopore wall [7]. The XRD patterns of the ZnO/Fe₃O₄/g-C₃N₄-x samples included all the typical peaks of g-C₃N₄, ZnO, and Fe₃O₄. The diffraction peaks located at 30.4° , 35.7° , and 43.4° correspond to the (220), (311), and (400) planes of Fe₃O₄ [18, 19]. Moreover, the peak intensity of the characteristic peak of g-C₃N₄ was gradually strengthened with an increase in the amount of g-C₃N₄, whereas the peak intensity of ZnO and Fe₃O₄ gradually decreased. No g-C₃N₄ characteristic peak was observed in the ZnO/Fe₃O₄/g-C₃N₄-20% samples, which can be attributed to the low content of the g-C₃N₄ in

the composite. From the XRD analysis results, no other peaks were observed in all the samples, thus confirming the high purity of the samples.

TEM and EDS

The structure of the sample was evaluated using TEM, as shown in Fig. 2. The TEM image of pure ZnO displays the typical hexagonal wurtzite structure (Fig. 2a), which is consistent with the XRD results. The TEM image of g-C₃N₄ (Fig. 2b) displays its layered platelet-like morphology structure, and smooth paper-fold thinner sheets, which is similar to the morphology of graphene nanosheets. As seen from the TEM image of ZnO/Fe₃O₄/g-C₃N₄-50% (Fig. 2c), a large amount of photocatalysts accumulated on the layered structure of g-C₃N₄. The EDS results for ZnO/Fe₃O₄/g-C₃N₄-50% are presented in Fig. 3. It can be seen that the sample contained peaks of Zn, C, N, Fe, and O elements, which also proved that the ZnO/Fe₃O₄/g-C₃N₄ composite was prepared successfully. However, the peak value of Fe is relatively low,

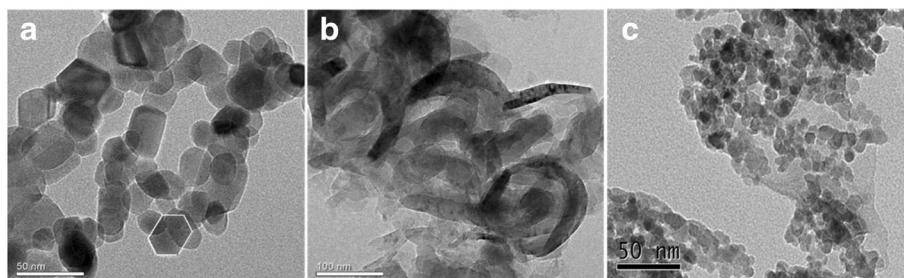


Fig. 2 TEM images of **a** ZnO, **b** g-C₃N₄, and **c** ZnO/Fe₃O₄/g-C₃N₄-50%

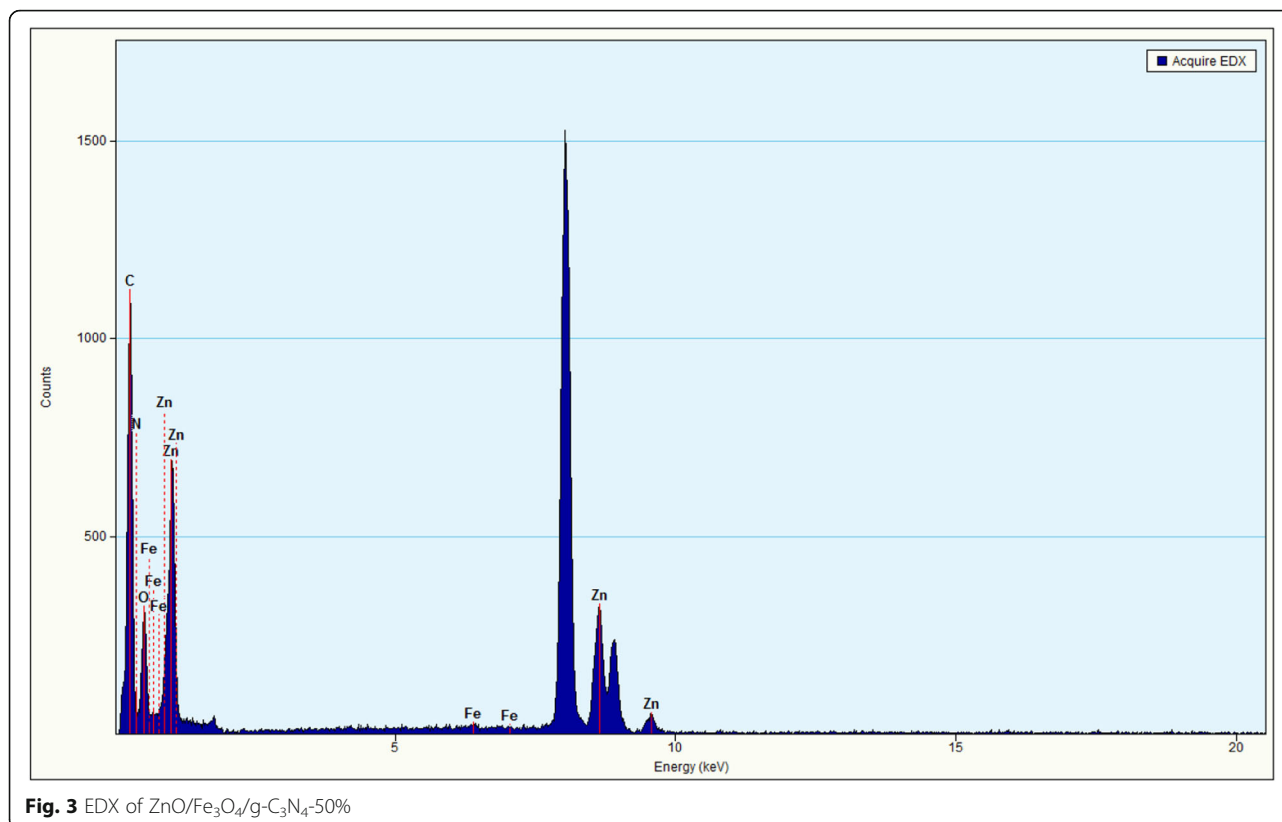


Fig. 3 EDX of ZnO/Fe₃O₄/g-C₃N₄-50%

suggesting that the content of Fe₃O₄ is low in ZnO/Fe₃O₄/g-C₃N₄ composites. Given that Cu was used as a carrier in the TEM analysis, characteristic peaks of Cu were detected in the EDS analysis [20].

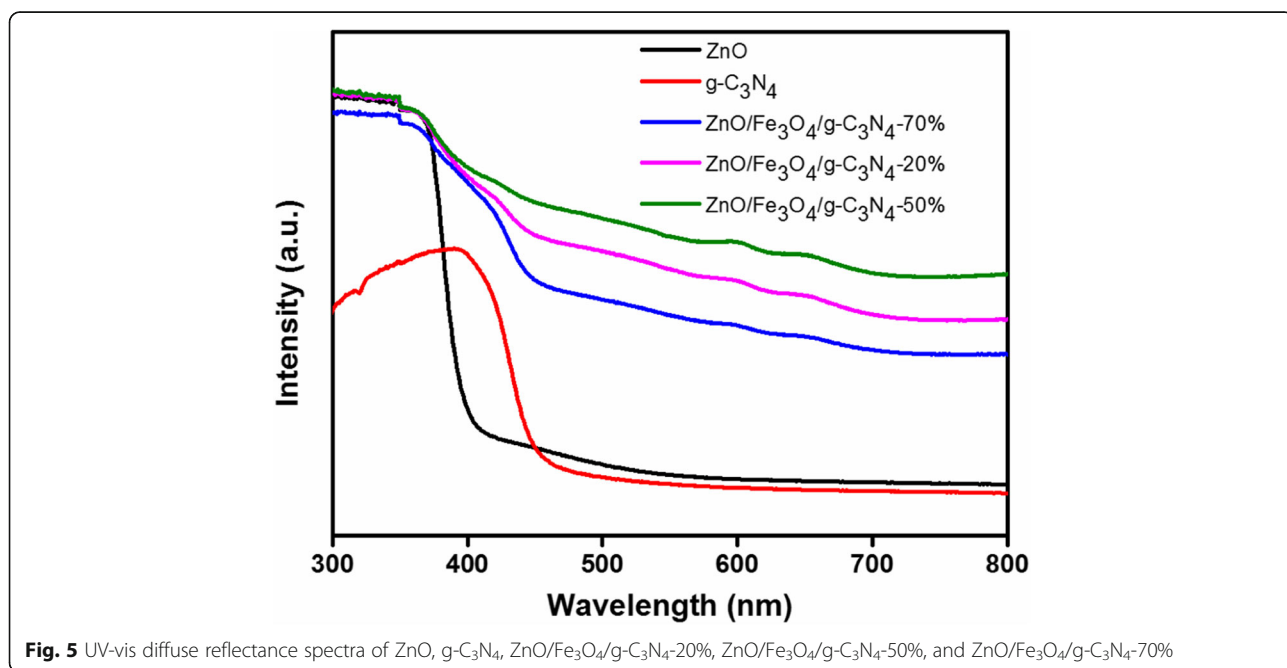
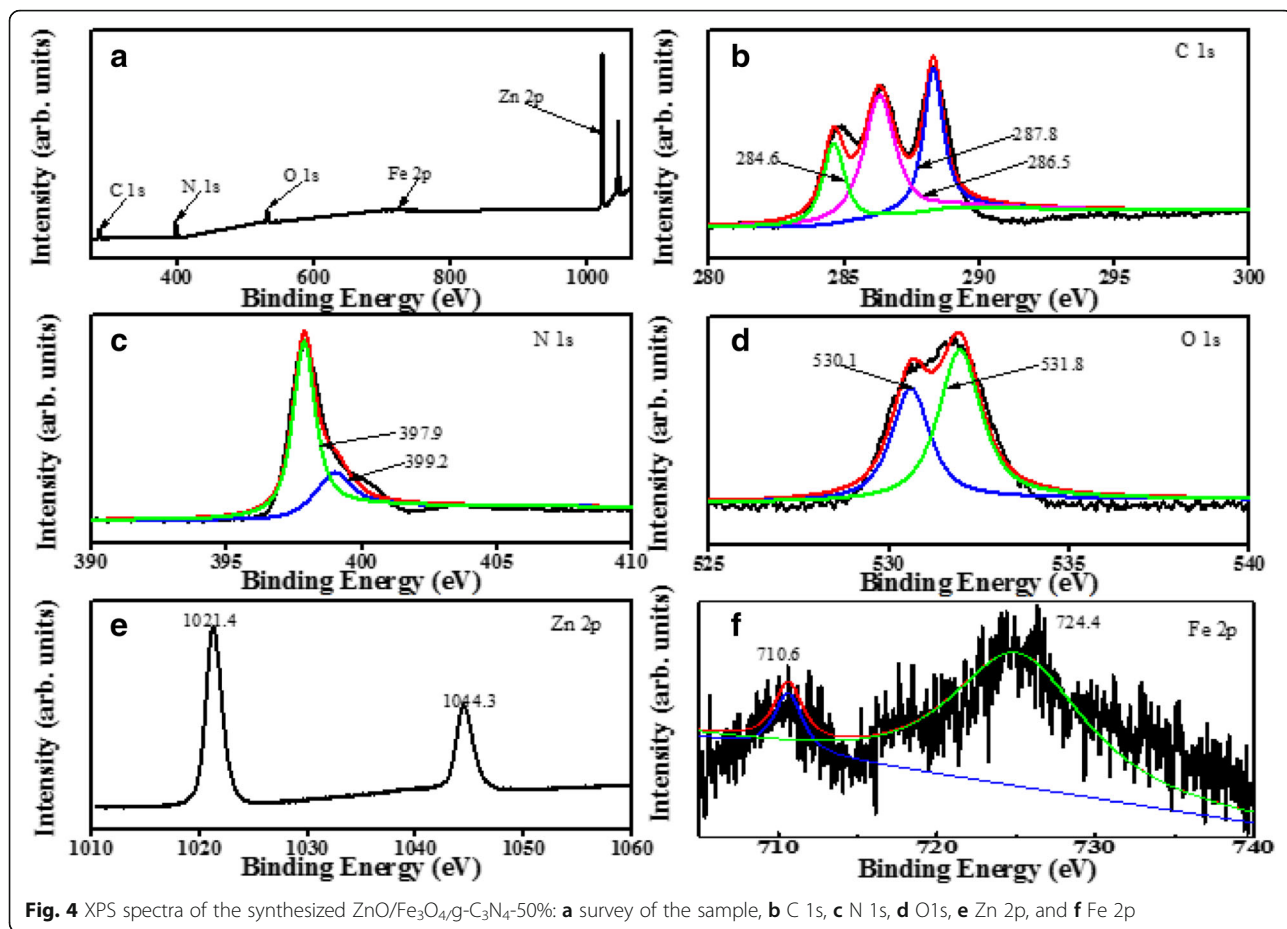
XPS

To investigate the surface composition and chemical states of the prepared composite catalysts, XPS was conducted on ZnO/Fe₃O₄/g-C₃N₄-50%. The survey spectrum scan reveals the presence of C, N, O, Zn, and Fe (Fig. 4a). Figure 4b reveals that the C 1s has three characteristic peaks. The peak located at 284.6 eV is attributed to the hydrocarbons in the XPS instrument and the sp²-hybridized carbon atoms in the aromatic ring, which were bonded to N (N–C=N). The other peak is attributed to the sp³ hybrid carbon source (C–(N)₃) with a binding energy of 286.5 eV. The peak at the binding energy of 287.8 eV is attributed to the C–N–C in the graphite phase [21]. The N 1s XPS spectrum is presented in Fig. 4c. A major peak was at 397.9 eV, which correspond to the aromatic between N and two C atoms (C=N–C). A weaker characteristic peak is located at 399.2 eV, which is mainly attributed to the trinitrogen (N–(C)₃) that links the basic structure (C₆N₇), or the amino groups related to the structural defects and incomplete condensation (C)₂–N–H [22]. The XPS spectrum of O 1s is presented in Fig. 4d, and the peak at

530.1 eV corresponds to the O₂[–] ion in the Zn–O bond of the ZnO hexagonal wurtzite structure [23]. The peak at 531.8 eV corresponds to the oxygen vacancy in ZnO. In the Zn 2p XPS spectrum (Fig. 4e), there are two characteristic peaks at the binding energies of 1021.4 eV and 1044.3 eV, and the distance between the two peaks is 22.9 eV, which is included in the standard reference value of zinc oxide. The binding energy difference indicates that the zinc ion in the composite was in +2 states [23]. In the XPS spectrum of the Fe 2p (Fig. 4f), the two peaks are located at 710.6 eV and 724.4 eV, which correspond to the 2p_{1/2} and 2p_{3/2} orbitals, respectively [24]. These results reveal that g-C₃N₄ are composited on the ZnO, which may promote the absorption of visible light and improve the transfer and separation of charge carriers; thus, enhancing the photocatalytic activity [25].

UV-vis DRS

Diffuse reflectance spectroscopy was used to investigate the light absorption behavior of the photocatalysts. The results are presented in Fig. 5. The absorption of light with a significant red shift may improve photocatalytic performance in the visible region. In the ultraviolet region, the pure ZnO demonstrated a strong absorption at the wavelength of 388 nm, which corresponds to a band gap of 3.20 eV. Different from the ZnO absorption behavior, g-C₃N₄ yields an absorption shift at 460 nm, and



the corresponding band gap energy was 2.70 eV, which indicates a higher response for photocatalytic activity under visible light [26]. Compared with pure ZnO or g-C₃N₄, the absorption edge of the ZnO/Fe₃O₄/g-C₃N₄ composite material shifted significantly to a longer wavelength region, which suggests that the absorption edge of the composite material shifted to the lower energy region. These results may be due to the synergistic relationship between g-C₃N₄ and ZnO in the composite samples, which is consistent with the report by Le et al. [7]. The red shift of the absorption edge of ZnO/Fe₃O₄/g-C₃N₄ increased with an increase in the g-C₃N₄ loading up to 50%. However, the absorption edge decreased, when the g-C₃N₄ loading was 70%. The decrease in ZnO/Fe₃O₄/g-C₃N₄-70% may be because g-C₃N₄ loading above the optimal level may shield the light intensity absorption by ZnO. Therefore, among all the prepared samples, the ZnO/Fe₃O₄/g-C₃N₄-50% composite exhibited the most extensive and strongest absorption of visible light. This is similar to the results obtained by Jo et al., who reported that ZnO-50%/g-C₃N₄ exhibited the strongest absorption of visible light [1]. The composite material demonstrated the strongest light absorption to visible light, which increased the generation of electron-hole pairs under visible light irradiation, resulting in a higher photocatalytic activity.

PL

The effect of the synergistic relationship between ZnO and g-C₃N₄ on the photocatalysis was further evaluated using PL. The PL spectra of ZnO, g-C₃N₄, and ZnO/Fe₃O₄/g-C₃N₄-50% are presented in Fig. 6. The excitation wavelength was 300 nm, and the PL of the samples

were tested at room temperature. The emission spectra in the range of 300–800 nm were recorded. It is common knowledge that the recombination of electron-hole pairs inside semiconductors releases energy in the form of PL. In general, a lower PL intensity indicates a lower recombination rate of carriers, which leads to efficient photocatalytic activity. In the PL spectrum, g-C₃N₄ exhibited a strong emission peak at approximately 460 nm, which is in accordance with the UV-vis results (Fig. 5) and literature [7]. The emission peak of pure ZnO was lower than that of g-C₃N₄, at approximately 410 nm [21]. Compared with the PL peak of pure ZnO, the emission peak of the ZnO/Fe₃O₄/g-C₃N₄-50% composite photocatalyst was red-shifted, and its peak intensity was significantly reduced. Moreover, PL peak intensity of the ZnO/Fe₃O₄/g-C₃N₄-50% composite photocatalyst was lowest. Based on these results, it was concluded that the electron-hole pairs photogenerated by the ZnO/Fe₃O₄/g-C₃N₄-50% nanocomposites under visible light irradiation can be effectively transferred at the interface of the heterostructure. Thus, the electron-hole recombination rate decreased, which resulted in the highest photocatalytic activity under visible light irradiation.

Electrochemical Analysis

The photocatalytic redox reactions between the separation, migration, and capture of photogenerated electrons by semiconductor photocatalysts are closely related. To qualitatively evaluate the photo-induced charge separation efficiency during the photocatalytic reaction, the photocurrent responses of the ZnO, g-C₃N₄, and ZnO/Fe₃O₄/g-C₃N₄-50% nanocomposites were investigated under visible light irradiation. Figure 7a

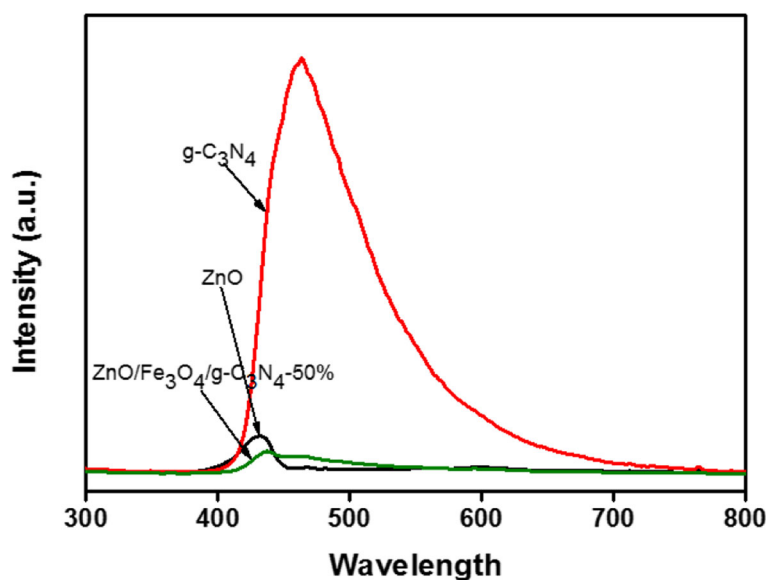
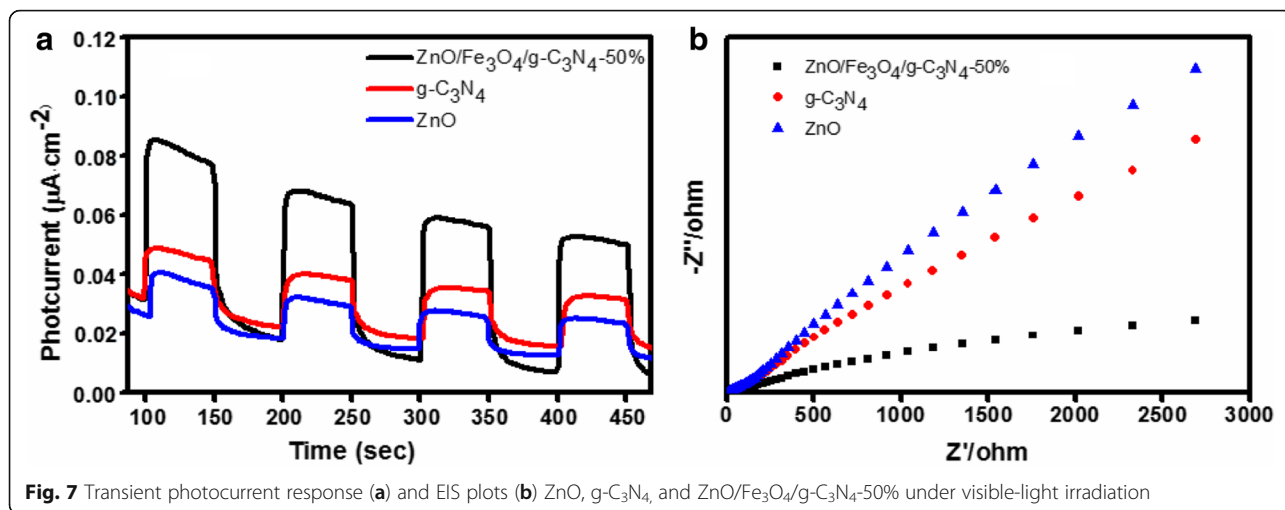


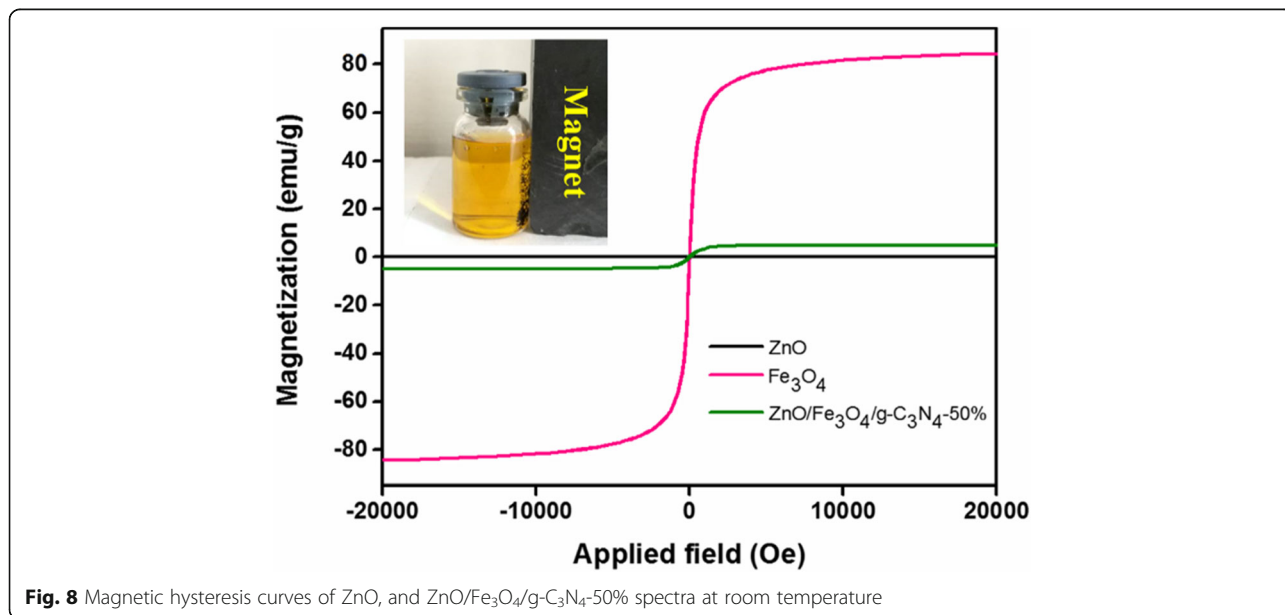
Fig. 6 PL spectra of ZnO, g-C₃N₄, and ZnO/Fe₃O₄/g-C₃N₄-50%



presents the photocurrent-time (I-t) curves of three samples under intermittent illumination. From the figure, it can be seen that once the irradiation of light was turned off, the photocurrent value decreased abruptly, and the photocurrent maintained a constant value when the light was turned on again. Moreover, this phenomenon is reproducible, which indicates that most of the photogenerated electrons were transferred to the surface of the sample, and a photocurrent was generated under visible light irradiation. Pure ZnO demonstrates the weakest photocurrent response under visible light irradiation, due to its wide band gap. Moreover, the ZnO/Fe₃O₄/g-C₃N₄-50% composite samples exhibited the highest photocurrent intensities. The results suggest that the relationship between ZnO and g-C₃N₄ is beneficial

for the improvement of the separation efficiency and transfer of photogenerated electrons and holes [27]. This phenomenon is consistent with the PL results.

The electrochemical impedance spectroscopy (EIS) results of the sample are presented in Fig. 7b. The arcs on the EIS electrochemical impedance spectrogram reflect the charge transfer layer resistance at the electrode/electrolyte interface. A smaller arc represents a lower resistance, which indicates a higher efficiency of charge transfer [27]. The arc radius of the ZnO/Fe₃O₄/g-C₃N₄-50% composite photocatalyst is smaller than that of ZnO and g-C₃N₄, which indicates that the charge transfer layer resistance of the ZnO/Fe₃O₄/g-C₃N₄-50% interface was the smallest. Thus, the photo-induced electron-hole pairs exhibited the highest separation and



transfer efficiency, which improved the photocatalytic activity. These results are consistent with the photocurrent results.

Magnetic Aroperties

The hysteresis loops of ZnO, Fe₃O₄, and ZnO/Fe₃O₄/g-C₃N₄-50% are presented in Fig. 8. The results reveal that pure ZnO is non-magnetic, pure Fe₃O₄ exhibited the strongest saturation magnetization, and the saturation magnetization of ZnO/Fe₃O₄/g-C₃N₄-50% was lower than that of the pure Fe₃O₄, which is attributed to the presence of non-magnetic substances, i.e., ZnO and g-C₃N₄. No hysteresis, remanence, and coercivity were observed in the hysteresis loop of ZnO/Fe₃O₄/g-C₃N₄-50%. Therefore, the sample was superparamagnetic. Moreover, the saturation magnetization of the composite photocatalyst was sufficient to separate from the solution using an external magnetic field, as shown in Fig. 8 (inset), which promoted the photocatalyst recovery and increased its recyclability.

Photocatalytic Properties

The degradation of MO over different photocatalysts is presented in Fig. 9a. The pure ZnO slightly degraded the methyl orange under visible light irradiation, given that the wide band gap of ZnO allows it to respond only to ultraviolet light. The degradation efficiency of pure g-C₃N₄ for methyl orange was not very high, due to its high photoelectron-hole pair recombination rate, despite its response to visible light, which resulted in the low photocatalytic activity of g-C₃N₄. The photodegradation efficiency of MO on the ZnO/Fe₃O₄/g-C₃N₄-50% composite photocatalyst was higher than that of the other catalysts, for the following three reasons: First, the UV-Vis spectra indicated that the ZnO/Fe₃O₄/g-C₃N₄-50% composite photocatalyst exhibited the strongest visible light response intensity and a large visible light absorption range. Second, the PL and electrochemical results revealed that the electron-hole pair recombination rate of ZnO/Fe₃O₄/g-C₃N₄-50% was the lowest. Third, the electrochemical results indicated that the photoelectron transfer rate of the ZnO/Fe₃O₄/g-C₃N₄-50% photocatalyst was the fastest compared with single photocatalyst.

In addition, the kinetics of the degradation of MO on the photocatalysts were also evaluated (Fig. 9b). The results revealed that the degradation kinetics of MO on different photocatalysts followed the first-order kinetic model, and all the degradation rate constants are presented in Table 2. The apparent rate constant of ZnO/Fe₃O₄/g-C₃N₄-50% was the highest (0.02430 min⁻¹), and which was higher than the degradation rate of g-C₃N₄/Fe₃O₄/TiO₂ and TiO₂/biochar composite

Table 2 First order kinetic constants and relative coefficients for photocatalytic degradation of MO over the samples

Samples	k (min ⁻¹)	R^2
ZnO	0.00006	0.9966
g-C ₃ N ₄	0.00369	0.9779
ZnO/Fe ₃ O ₄ /g-C ₃ N ₄ -20%	0.01023	0.9827
ZnO/Fe ₃ O ₄ /g-C ₃ N ₄ -50%	0.02430	0.9904
ZnO/Fe ₃ O ₄ /g-C ₃ N ₄ -70%	0.00778	0.9819

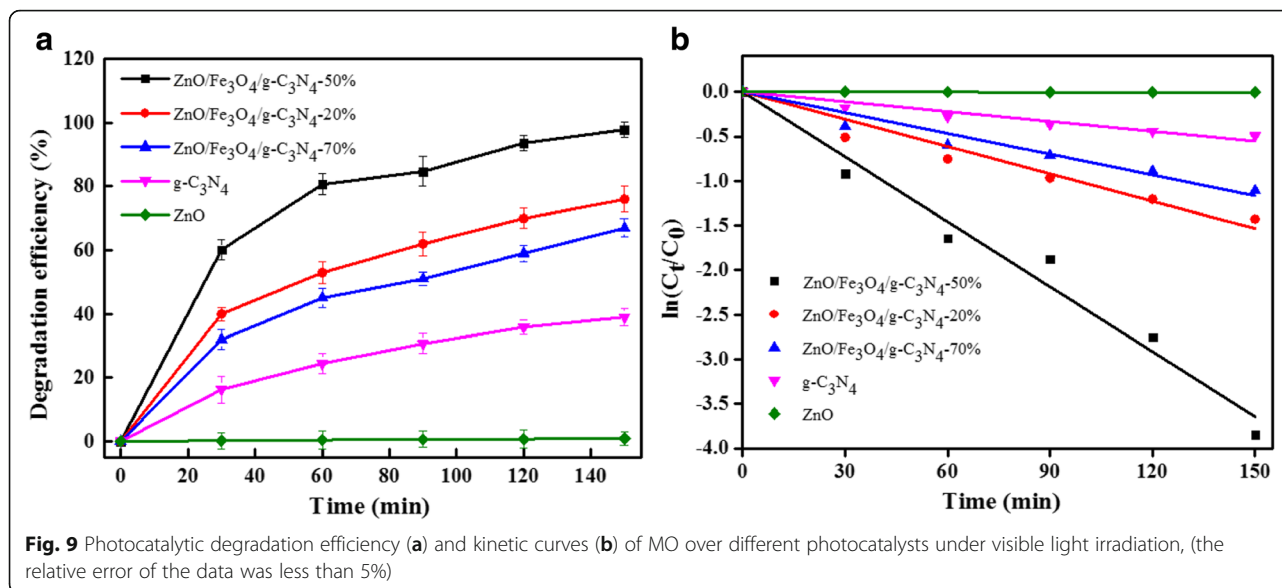
catalysts [28, 29]. Moreover, the ZnO/Fe₃O₄/g-C₃N₄-50% exhibited a higher photocatalytic rate relative to g-C₃N₄/Fe₃O₄/AgI on the degradation of MO (0.0016 min⁻¹) [10].

Stability of ZnO/Fe₃O₄/g-C₃N₄-50% Composite Photocatalyst

In addition, the stability of photocatalysts is a critical factor in relation to large-scale technology application. To evaluate the stability of the ZnO/Fe₃O₄/g-C₃N₄-50% composite photocatalyst, recycling experiments were conducted on the photocatalyst for the degradation of MO under visible light irradiation. The photocatalyst was collected by magnetic decantation and then washed using distilled water and ethanol. Thereafter, it was dried in an oven at 80 °C. The sample was reused for subsequent degradation, and the results are presented in Fig. 10a. The composite photocatalyst maintained a very high photocatalytic activity, and the removal rate of MO on the ZnO/Fe₃O₄/g-C₃N₄-50% composite photocatalyst was 95.3% after 5 cycles. In addition, there was a slight decrease in the amount of photocatalysts during the cycle processes. Therefore, the ZnO/Fe₃O₄/g-C₃N₄-50% composite photocatalyst exhibited high stability under visible light irradiation. To further evaluate the stability of the ZnO/Fe₃O₄/g-C₃N₄-50%, samples were collected after 5 cycles for XRD testing and compared with the XRD pattern of the sample before cycling. The results are presented in Fig. 10b. No significant changes were observed in the structure of the photocatalyst before and after use, which indicates that the ZnO/Fe₃O₄/g-C₃N₄-50% photocatalyst was highly stable.

Degradation of Monoazo Dyes on ZnO/Fe₃O₄/g-C₃N₄-50%

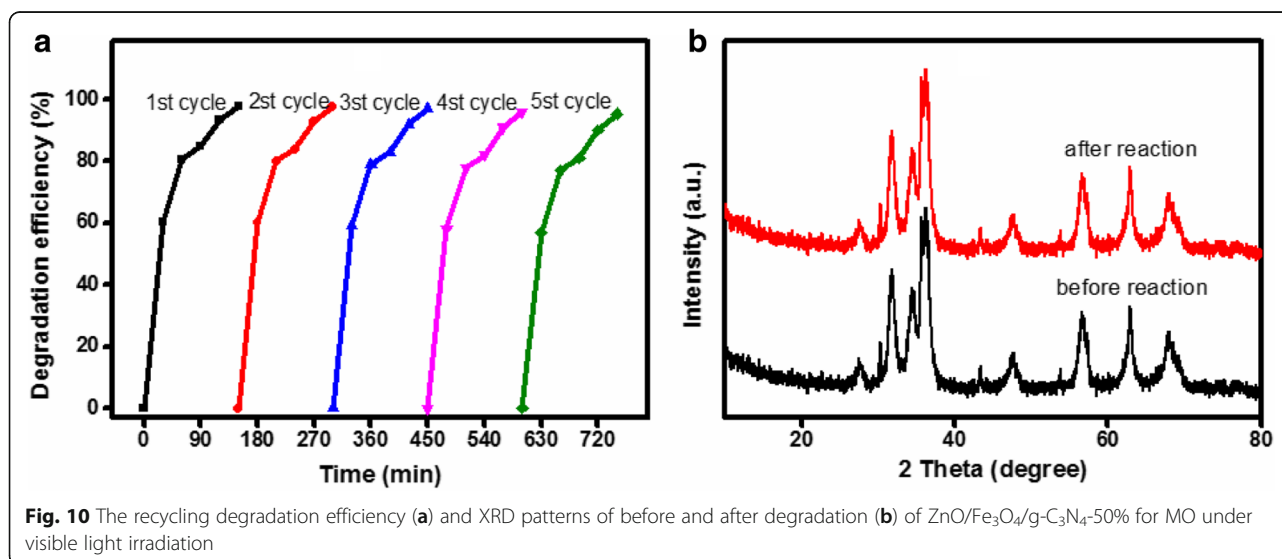
For the evaluation of the photocatalytic degradation behavior of different monoazo dyes, the degradation of MO, AYR, and OG over ZnO/Fe₃O₄/g-C₃N₄ is presented in Fig. 11. The plots of the absorbance with respect to the wavelength for the MO, AYR, and OG degradations over ZnO/Fe₃O₄/g-C₃N₄-50% at various irradiation times are presented in Figs. 11a–c. The maximum absorption wavelength of MO, AYR, and OG before and after degradation were 466 nm, 372 nm, and

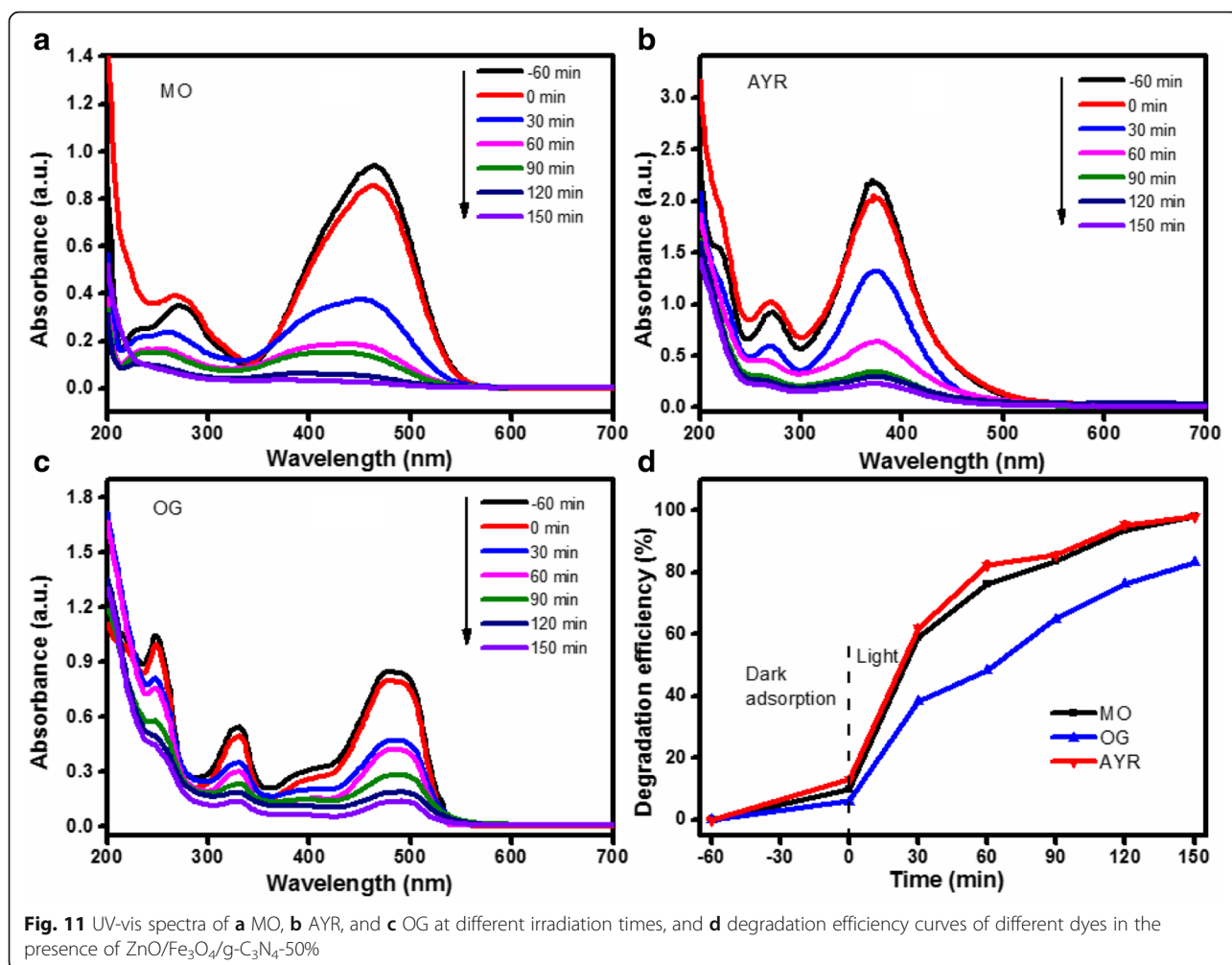


475 nm, respectively. With the gradual extension of the illumination time to 150 min, the intensity of the absorption peak gradually decreased, implying the gradual mineralization of MO, AYR, and OG. Furthermore, under visible-light irradiation for 150 min, the degradation efficiencies of MO, AYR, and OG were 97.87%, 98.05%, and 83.35%, respectively (Fig. 11d). There are two possible reasons for this phenomenon. First, as can be seen in Fig. 11d, the adsorption efficiency of OG on the photocatalyst was the lowest. The lower adsorption efficiency of OG can be explained by the steric limit of a large aromatic molecule, which reduced the number of OG molecules adsorbed on the photocatalyst. The lower adsorption efficiency of the azo dye therefore resulted in a small amount of molecules concentrated on the active

site of the photocatalyst, which decreased the degradation efficiency of the azo dye [30]. Second, AYR has a high degradation efficiency, which is related to the presence of a carboxyl group that can react with H⁺ in a light Kolbe reaction. However, the lower degradation efficiency of OG and MO could be due to the presence of a withdrawing SO₃⁻ group, and the increasing number of sulfonic acid groups could inhibit degradation of the dye [31]. The properties of the three dyes are listed in Table 1. The molecular weight and number of sulfonic acid was in the following order: AYR < MO < OG. Therefore, the degradation efficiency of OG over ZnO/Fe₃O₄/g-C₃N₄-50% was the lowest.

It is necessary to investigate the relationship between the molecular weight of the azo dye and its degradation





efficiency. Figure 12 reveals that the molecular weight of azo dye had a good negative correlation with the degradation efficiency ($R^2 = 0.9776$). Moreover, a molecular weight of the azo dye would result in a low degradation efficiency. The results are consistent with those presented above.

Mechanism for Photocatalytic Degradation

To further investigate the mechanism of the photocatalyst for the degradation of MO under visible light irradiation, radical, electron, and hole scavenging experiments were conducted to detect the main active species in the photocatalytic process. Moreover, $\cdot\text{OH}$, $\cdot\text{O}_2^-$, h^+ , and e^- were eliminated using tert-butanol (*t*-BuOH), *p*-benzoquinone (*p*-BQ), ammonium oxalate (AO), and $\text{K}_2\text{S}_2\text{O}_8$, respectively. The degradation efficiencies of MO on the photocatalyst in the presence of the scavengers are presented in Fig. 13. The removal rate of MO was significantly reduced after the addition of *t*-BuOH and *p*-BQ. Conversely, the removal efficiency of MO was not significantly reduced in the presence of AO and $\text{K}_2\text{S}_2\text{O}_8$.

Therefore, the active species that play a critical role during the photocatalytic degradation of MO over the ZnO/Fe₃O₄/g-C₃N₄-50% photocatalyst are $\cdot\text{OH}$ and $\cdot\text{O}_2^-$.

Based on the relevant literature and experimental results (including the physicochemical properties, photocatalytic performance, and detected active components), a possible photocatalytic mechanism of the ZnO/Fe₃O₄/g-C₃N₄-50% nanocomposites prepared under visible light irradiation is proposed. It is common knowledge that ZnO and g-C₃N₄ are typical n-type semiconductors. Therefore, an n-n heterojunction is formed at the interface between the g-C₃N₄ and ZnO nanoparticles. The ZnO/Fe₃O₄/g-C₃N₄-50% can be excited to generate electrons and holes under visible light irradiation. The excited electrons are then transferred from the CB of the g-C₃N₄ to the CB of the ZnO. The improvement of the photocatalytic performance of the composite photocatalyst is mainly due to the effective separation of photo-generated electrons and holes at the heterojunction interface [32]. Given that the CB edge potential of g-C₃N₄ is more negative than that of ZnO, the excited

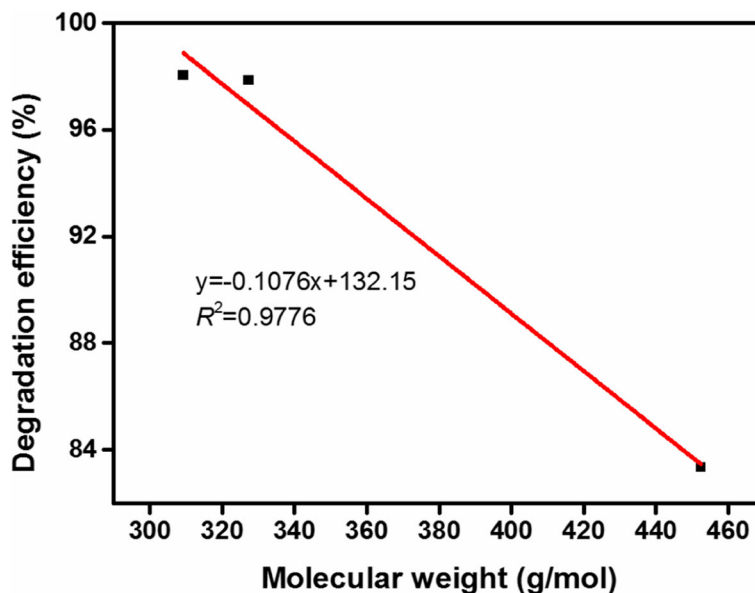
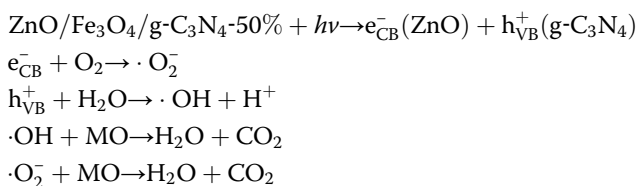


Fig. 12 Correlation between molecular weight of azo dye and degradation efficiency

electrons in g-C₃N₄ are transferred to the CB of ZnO, and the holes are retained in the valence band (VB) of g-C₃N₄ [33, 34]. In contrast, ZnO holes are injected into the holes of g-C₃N₄. Therefore, an internal electrostatic potential is formed in the space charge region, which promotes the separation of the photogenerated carriers. The charge transfer to the surface of the compound semiconductor reacts with water and dissolved oxygen to produce ·OH and ·O₂⁻, or it reacts directly with MO. From Fig. 13, it can be seen that ·OH and ·O₂⁻ play a vital role in the degradation of MO on composite

photocatalysts. Therefore, possible photocatalytic mechanisms are presented below:



Based on the above discussion, it was concluded that the photocatalytic activity of the ZnO/Fe₃O₄/g-C₃N₄-50%

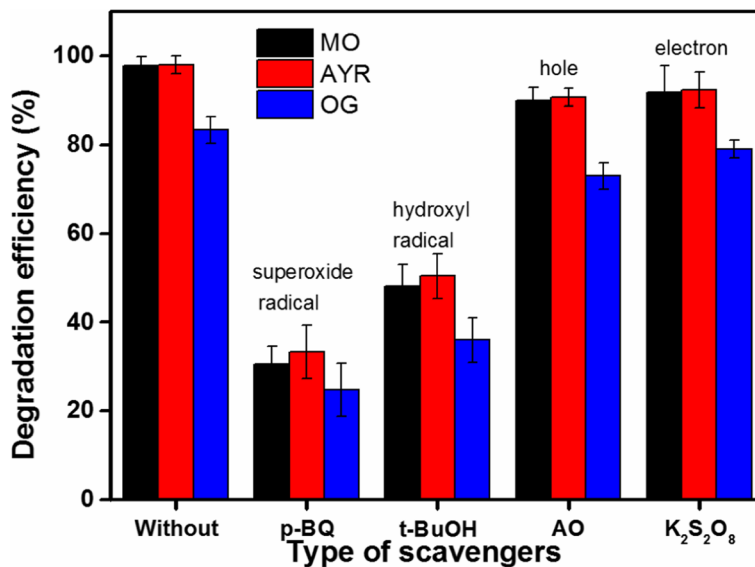


Fig. 13 The degradation efficiencies of monazo dyes over ZnO/Fe₃O₄/g-C₃N₄-50% in the presence of various scavengers

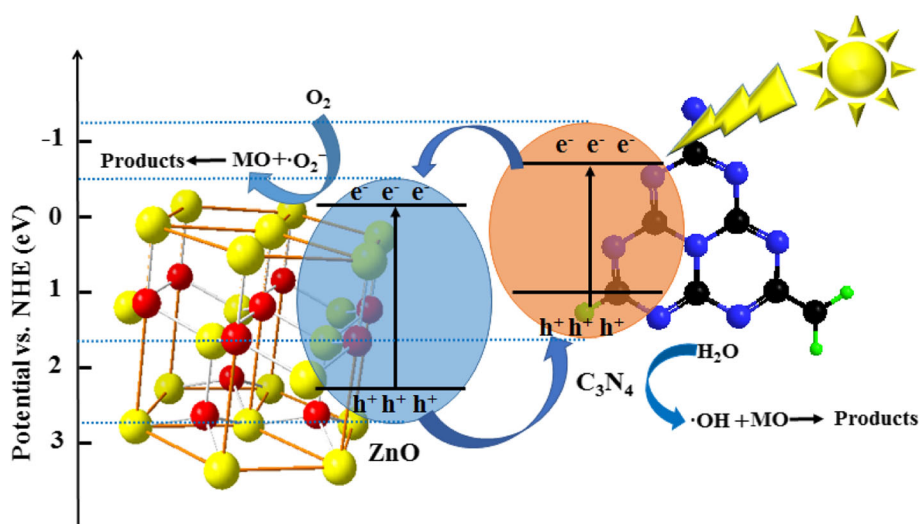


Fig. 14 Mechanism for photocatalytic degradation of monazo dyes on the ZnO/Fe₃O₄/g-C₃N₄-50% photocatalyst

nanocomposite semiconductor was significantly improved. This was because of the following two reasons: (1) heterostructure between g-C₃N₄ and ZnO improved the light absorption properties, and (2) the synergistic effect of the internal electric field and the matched band structure of g-C₃N₄ and ZnO increased the separation rate of photo-generated carriers (Fig. 14).

Conclusions

In this study, ternary magnetic ZnO/Fe₃O₄/g-C₃N₄ nanocomposites were successfully fabricated, as novel recyclable visible-light-driven photocatalysts. Among all the prepared photocatalysts, the ZnO/Fe₃O₄/g-C₃N₄-50% composite photocatalyst exhibited the most efficient photocatalytic activity, due to the improved light absorption properties resulting from the heterojunction structure between g-C₃N₄ and ZnO, in addition, to the synergistic effect of their internal electric field and matched energy band structure. Moreover, the separation rate of the photogenerated carriers was high. The degradation efficiencies of MO, AYR, and OG over ZnO/Fe₃O₄/g-C₃N₄-50% were 97.87%, 98.05%, and 83.35%. This was due to the number of dye molecule adsorbed on the photocatalyst, and the structure of the azo dye molecule had an influence on the degradation. The kinetics of the degradation of MO on the composite photocatalyst was in accordance with first-order kinetics. Furthermore, the addition of Fe₃O₄ significantly improved the stability and recyclability of the photocatalyst. Superoxide ions are the main reactive species, which indicates that the azo dyes have the same degradation mechanism.

Abbreviations

AO: Ammonium oxalate; AYR: Alizarin yellow R; CB: Conduction band; DRS: Diffuse reflectance spectroscopy; EDS: Energy dispersive X-ray spectroscopy; EIS: Electrochemical impedance spectroscopy; EtOH: Ethanol; Fe₃O₄: Ferroferric oxide; g-C₃N₄: Graphite-like carbon nitride; MO: Methyl orange; OG: Orange G; *p*-BQ: *p*-Benzoquinone; PL: Photoluminescence spectra; *t*-BuOH: Tert-butanol; TEM: Transmission electron microscopy; UV: Ultraviolet; VB: Valence band; VSM: Vibrating sample magnetometry; XRD: X-ray diffraction; ZnO: Zinc oxide

Acknowledgements

We acknowledge the support from the National Natural Science Foundation of China (21868034) and the International Science and Technology Cooperation Program of Shihezi University (GJHZ201601).

Funding

The National Natural Science Foundation of China (21868034) and the International Science and Technology Cooperation Program of Shihezi University (GJHZ201601).

Availability of Data and Materials

The datasets used and/or analyzed during the current study are available from the corresponding author on reasonable request.

Authors' Contributions

ZW guided the design, analyzed the data, and drafted the manuscript. XC and XL performed the experiments and discussed the results. XY and YY performed the characterization of the samples. All authors contributed to the revision of the manuscript. All authors read and approved the final manuscript.

Competing Interests

The authors declare that they have no competing interests.

Publisher's Note

Springer Nature remains neutral with regard to jurisdictional claims in published maps and institutional affiliations.

Received: 27 December 2018 Accepted: 4 April 2019

Published online: 29 April 2019

References

- Xue YT, Du CF, Wu ZS, Zhang LH (2018) Relationship of cellulose and lignin contents in biomass to the structure and RB-19 adsorption behavior of activated carbon. *New J. Chem.* 42:16493–16502
- Zhang C, Li Y, Shuai DM, Shen Y, Wang DW (2019) Progress and challenges in photocatalytic disinfection of waterborne viruses: a review to fill current knowledge gaps. *Chem. Eng. J.* 355:399–415
- Tian F, Wu ZS, Chen QY, Yan YJ, Cravotto G, Wu ZL (2015) Microwave-induced crystallization of AC/TiO₂ for improving the performance of rhodamine B dye degradation. *Appl. Surf. Sci.* 351:104–112
- Prasad GK, Ramacharyulu P, Singh B, Batra K, Srivastava AR, Ganesan K, Vijayaraghavan R (2011) Sun light assisted photocatalytic decontamination of sulfur mustard using ZnO nanoparticles. *J Mol Catal A-Chem* 349:55–62
- Wang J, Chen R, Xiang L, Komarneni S (2018) Synthesis, properties and applications of ZnO nanomaterials with oxygen vacancies: a review. *Ceram. Int.* 44(7):7357–7377
- Wang XJ, Song JK, Huang JY, Zhang J, Wang X, Ma RR, Wang JY, Zhao JF (2016) Activated carbon-based magnetic TiO₂ photocatalyst co-doped with iodine and nitrogen for organic pollution degradation. *Appl. Surf. Sci.* 390:190–201
- Le SK, Jiang TS, Li YW, Zhao Q, Li YY, Fang WB, Gong M (2017) Highly efficient visible-light-driven mesoporous graphitic carbon nitride/ZnO nanocomposite photocatalysts. *Appl Catal B: Environ* 200:601–610
- Thi VHT, Lee BK (2017) Great improvement on tetracycline removal using ZnO rod-activated carbon fiber composite prepared with a facile microwave method. *J Hazard Mater* 324:329–339
- Bhirud A, Sathaye S, Waichal R, Park CJ, Kale B (2015) In situ preparation of N-ZnO/graphene nanocomposites: excellent candidate as a photocatalyst for enhanced solar hydrogen generation and high performance supercapacitor electrode. *J Mater Chem A* 3:17050–17063
- Akhundi A, Habibi-Yangjeh A (2016) Ternary magnetic g-C₃N₄/Fe₃O₄/AgI nanocomposites: novel recyclable photocatalysts with enhanced activity in degradation of different pollutants under visible light. *Mater Chem Phys* 174:59–69
- Chen XQ, Wu ZS, Gao ZZ, Ye BC (2017) Effect of different activated carbon as carrier on the photocatalytic activity of Ag-N-ZnO photocatalyst for methyl orange degradation under visible light irradiation. *Nanomaterials* 7(9):258–260
- Huang DL, Yan XL, Yan M, Zeng GM, Zhou CY, Wan J, Cheng M, Xue WJ (2018) Graphitic carbon nitride based heterojunction photoactive nanocomposites: applications and mechanism insight. *ACS Appl. Mater. Interfaces* 10(25):21035–21055
- Mousavi M, Habibi-Yangjeh A (2016) Magnetically separable ternary g-C₃N₄/Fe₃O₄/BiOI nanocomposites: Novel visible-light-driven photocatalysts based on graphitic carbon nitride. *J Colloid Interface Sci* 465:83–92
- Cao JJ, Gong YX, Wang Y, Zhang B, Zhang HL, Sun G, Hari B, Zhang ZY (2017) Cocoon-like ZnO decorated graphitic carbon nitride nanocomposite: hydrothermal synthesis and ethanol gas sensing application. *Mater Lett* 198:76–80
- Xue YT, Wu ZS, He XF, Yang X, Chen XQ, Gao ZZ (2019) Constructing a Z-scheme heterojunction of egg-like core@ shell CdS@ TiO₂ photocatalyst via a facile reflux method for enhanced photocatalytic performance. *Nanomaterials* 9(2):222–237
- Saffari J, Mir N, Ghanbari D, Khandan-Barani K, Hassanabadi A, Hosseini-Tabatabaei MR (2015) Sonochemical synthesis of Fe₃O₄/ZnO magnetic nanocomposites and their application in photo-catalytic degradation of various organic dyes. *J Mater Sci: Mater Electron* 26:9591–9599
- Chen XQ, Wu ZS, Liu DD, Gao ZZ (2017) Preparation of ZnO photocatalyst for the efficient and rapid photocatalytic degradation of azo dyes. *Nanoscale Res. Lett.* 12:143
- Shekofteh-Gohari M, Habibi-Yangjeh A (2016) Ultrasonic-assisted preparation of novel ternary ZnO/AgI/Fe₃O₄ nanocomposites as magnetically separable visible-light-driven photocatalysts with excellent activity. *J Colloid Interface Sci* 44:144–153
- Wu SH, Wu JL, Jia SY, Chang QW, Ren HT, Liu Y (2013) Cobalt (II) phthalocyanine-sensitized hollow Fe₃O₄@SiO₂@TiO₂ hierarchical nanostructures: fabrication and enhanced photocatalytic properties. *Appl. Surf. Sci.* 287:389–396
- Bian X, Hong K, Liu L, Xu M (2013) Magnetically separable hybrid CdS-TiO₂-Fe₃O₄ nanomaterial: enhanced photocatalytic activity under UV and visible irradiation. *Appl. Surf. Sci.* 280:349–353
- Deng YR, Liu KW, Cao HM, Luo ML, Yan HJ (2015) Synthesis of graphene with both high nitrogen content and high surface area by annealing composite of graphene oxide and g-C₃N₄. *J. Iran. Chem. Soc.* 12:807–814
- Wang WG, Cheng B, Yu JG, Liu G, Fan WH (2012) Visible-light photocatalytic activity and deactivation mechanism of Ag₃PO₄ spherical particles. *Chem-Asian J* 7:1902
- Kotsis K, Staemmler V (2006) Ab initio calculations of the O1s XPS spectra of ZnO and Zn oxo compounds. *Phys Chem Chem Phys* 8:1490–1498
- Lin X, Wang X, Zhou Q, Wen C, Su S, Xiang J, Gao X (2018) Magnetically recyclable MoS₂/Fe₃O₄ hybrid composite as visible light responsive photocatalyst with enhanced photocatalytic performance. *ACS Sustainable Chem Eng* 7(1):1673–1682
- Yu WL, Xu DF, Peng TY (2015) Enhanced photocatalytic activity of g-C₃N₄ for selective CO₂ reduction to CH₃OH via facile coupling of ZnO: a direct Z-scheme mechanism. *J Mater Chem A* 3:19936–19947
- Zhu Z, Huo P, Lu Z, Yan Y, Liu Z, Sh W, Dong H (2018) Fabrication of magnetically recoverable photocatalysts using g-C₃N₄ for effective separation of charge carriers through like-Z-scheme mechanism with Fe₃O₄ mediator. *Chem Eng J* 331:615–625
- Bu YY, Chen ZY, Li WB (2014) Using electrochemical methods to study the promotion mechanism of the photoelectric conversion performance of Ag-modified mesoporous g-C₃N₄ heterojunction material. *Appl Catal B: Environ* 144:622–630
- Wei XN, Wang HL (2018) Preparation of magnetic g-C₃N₄/Fe₃O₄/TiO₂ photocatalyst for visible light photocatalytic application. *J. Alloys Compd.* 763:844–853
- Lu L, Shan R, Shi Y, Wang S, Yuan H (2019) A novel TiO₂/biochar composite catalysts for photocatalytic degradation of methyl orange. *Chemosphere.* 222:391–398
- Lachheb H, Puzenat E, Houas A, Ksibi M, Elaloui E, Guillard C, Herrmann JM (2002) Photocatalytic degradation of various types of dyes (Alizarin S, Crocein Orange G, Methyl Red, Congo Red, Methylene Blue) in water by UV-irradiated titania. *Appl Catal B: Environ* 39:75–90
- Guillard C, Lachheb H, Houas A, Ksibi M, Elaloui E, Herrmann JM (2003) Influence of chemical structure of dyes, of pH and of inorganic salts on their photocatalytic degradation by TiO₂: comparison of the efficiency of powder and supported TiO₂. *J Photochem Photobiol A* 158:27–36
- Zhu YP, Li M, Liu YL, Ren TZ, Yuan ZY (2014) Carbon-doped ZnO hybridized homogeneously with graphitic carbon nitride nanocomposites for photocatalysis. *J. Phys. Chem. C.* 118:10963–10971
- Kochuveedu ST, Jang YH, Jiang YJ, Kim DH (2013) Visible light active photocatalysis on block copolymer induced strings of ZnO nanoparticles doped with carbon. *J Phys Chem A* 18:898–905
- Liu G, Niu P, Sun CH, Smith SC, Chen ZG, Lu GQ, Cheng HM (2010) Unique electronic structure induced high photoreactivity of sulfur-doped graphitic C₃N₄. *J Am Chem Soc* 132:11642–11648

Submit your manuscript to a SpringerOpen[®] journal and benefit from:

- Convenient online submission
- Rigorous peer review
- Open access: articles freely available online
- High visibility within the field
- Retaining the copyright to your article

Submit your next manuscript at ► [springeropen.com](https://www.springeropen.com)